URBAN MONITORING BASED ON SENTINEL-1 DATA USING PERMANENT SCATTERER INTERFEROMETRY AND SAR TOMOGRAPHY

M. Crosetto[1,*], A. Budillon[2], A. Johnsy[2], G. Schirinzi[2], N. Devanthéry[1], O. Monserrat[1], M. Cuevas-González[1]

[1] Centre Tecnològic de Telecomunicacions de Catalunya (CTTC/CERCA), Geomatics Division, Av. Gauss, 7, E-08860 Castelldefels (Barcelona), Spain (mcrosetto, ndevanthery, omonserrat, mcuevas)@cttc.cat
[2] Dipartimento di Ingegneria, Università degli Studi di Napoli "Parthenope", Centro Direzionale, Isola C4, 80143 Naples, Italy (alessandra.budillon, angel.johnsy, gilda.schirinzi)@uniparthenope.it

Commission III, WG III/3

KEY WORDS: SAR, Sentinel-1, Interferometry, Persistent Scatterer Interferometry, SAR tomography, inter-comparison.

ABSTRACT:

A lot of research and development has been devoted to the exploitation of satellite SAR images for deformation measurement and monitoring purposes since Differential Interferometric Synthetic Apertura Radar (InSAR) was first described in 1989. In this work, we consider two main classes of advanced DInSAR techniques: Persistent Scatterer Interferometry and Tomographic SAR. Both techniques make use of multiple SAR images acquired over the same site and advanced procedures to separate the deformation component from the other phase components, such as the residual topographic component, the atmospheric component, the thermal expansion component and the phase noise. TomoSAR offers the advantage of detecting either single scatterers presenting stable proprieties over time (Persistent Scatterers) and multiple scatterers interfering within the same range-azimuth resolution cell, a significant improvement for urban areas monitoring. This paper addresses a preliminary inter-comparison of the results of both techniques, for a test site located in the metropolitan area of Barcelona (Spain), where interferometric Sentinel-1 data were analysed.

1. INTRODUCTION

The first description of Differential Interferometric Synthetic Aperture Radar (DInSAR) was based on L-band Seasat data and was made by Gabriel et al. (1989). In almost three decades, there has been a lot of research related to the exploitation of SAR images to derive deformation measurements. The DInSAR technique has been successfully exploited for a wide range of application fields, achieving important scientific and technical results. For a review, see Bamler and Hartl (1998) and Rosen et al. (2000).

Several advanced DInSAR techniques have been proposed since the nineties, e.g. see Ferretti et al. (2001), Strozzi et al. (2009), Crosetto et al. (2010), Gernhardt and Bamler (2012), Devanthéry et al (2014), Huang et al (2017). In this paper we refer to them as Persistent Scatterer Interferometric techniques, see for a general review Crosetto et al. (2016). The common characteristic of the PSI techniques is the use of multiple SAR images acquired over the same site and advanced procedures to separate the deformation component from the other phase components (e.g. residual topographic component, atmospheric component and phase noise).

Tomographic SAR (TomoSAR) techniques have been proposed in the last decade, e.g. see Fornaro and Pascazio (2013) and Baselice et al. (2014). TomoSAR offers the advantage of detecting either single scatterers presenting stable proprieties over time (Persistent Scatterers or PS), as well as multiple scatterers interfering within the same range-azimuth resolution cell. This advantage is particularly useful for urban areas monitoring.

This paper describes two complementary techniques: a PSI technique implemented at CTTC (Spain), and a TomoSAR approach implemented at the Naples University "Parthenope" (Italy). Then it addresses a preliminary inter-comparison of the results of both techniques. The inter-comparison results refer to a test site located in the metropolitan area of Barcelona, where interferometric Sentinel-1 data were analysed.

2. A PSI TECHNIQUE

The PSI model to estimate the residual topographic error (*RTE*), the displacement rate (v) and the thermal expansion is briefly discussed in this section, see for details Biescas et al. (2007) and Monserrat et al. (2011). The model is:

$$\Delta\Phi_e^k = \frac{4\pi}{\lambda}\Delta T^k \Delta v_e + \frac{4\pi}{\lambda}\frac{B_\perp^k}{R_e^k sen\theta_e^k}\Delta RTE_e + \frac{4\pi}{\lambda}\Delta Temp^k \Delta Th_e + \Delta\Phi res_e^k \quad (1)$$

where $\Delta\Phi_e^k$ is the differential interferometric wrapped phase, where k is the interferogram number, e the edge that connects two PSs and Δ indicates the difference of the phases of the two PSs. The first component is the deformation velocity component, where Δv_e is the unknown differential velocity associated with e, ΔT^k is the temporal baseline of interferogram k and λ is the radar wavelength. The second component is the *RTE* component, where ΔRTE_e is the differential *RTE* associated with e, while $B_\perp^k$, R_e^k and θ_e^k are the normal baseline, the slant range and incidence angle of interferogram k, respectively. The third component is the

* Corresponding author

thermal expansion component, where $\Delta Temp^k$ is the temperature difference at the time of acquisition of the two images of interferogram k and ΔTh_e is the differential thermal expansion parameter associated with e. The last term, $\Delta\Phi res_e^k$, is the residual phase component.

The deformation velocity map is obtained by integrating the Δv_e values. The RTE map is obtained by integrating the ΔRTE_e values. Finally, the thermal map is obtained by integrating the ΔTh_e values.

3. A TOMOGRAPHYC SAR TECHNIQUE

TomoSAR is a multidimensional imaging technique that can be used to localize scatterers, reconstructing the topography and estimating the displacements of the observed scene (Baselice et al., 2014). The displacements can be divided into two categories: those that depend on the time and those that are related to temperature changes (thermal expansion). TomoSAR makes use of a stack of complex SAR images to discriminate the superimposed scatterers in a given range-azimuth cell by synthesizing an elevation aperture to reconstruct a full 3D reflectivity profile along azimuth, range and elevation. We briefly outline below a TomoSAR technique called TomoSAR Fast-Sup-GLRT (Budillon et al., 2016, 2017a, 2017b).

The TomoSAR techniques exploit both the amplitude and the phase information contained in the received signal. In any azimuth-range pixel, the k-th image u_k, acquired with different temporal baselines ΔT^k, different orthogonal baselines $B_\perp^k$, and temperature differences $\Delta Temp^k$, is given by the coherent superposition of the reflectivity of all the scatterers located at the same range-azimuth resolution cell and with different elevation position ΔRTE, differential deformation velocity Δv and differential thermal parameter ΔTh.

We can denote with $\boldsymbol{\gamma}$ the $N\times1$ (complex valued) column vector whose elements are the samples of the reflectivity at different elevations for a fixed range and azimuth position, thus, the sampled received signal is related to $\boldsymbol{\gamma}$ by:

$$\mathbf{u} = \boldsymbol{\Phi}\boldsymbol{\gamma} + \mathbf{w} \tag{2}$$

where $\mathbf{u}$ is an $M\times1$ observation (complex valued) column vector, $\mathbf{w}$ is an $M\times1$ column vector representing noise and clutter, and $\boldsymbol{\Phi}$ is an $M\times N$ measurement matrix related to the acquisition geometry, whose m-th row $\boldsymbol{\phi}_m$ is given by $vec(\boldsymbol{\Phi}_{m3})$, where vec is the operator transforming a three-dimensional matrix of size $N_s\times N_v\times N_k$ in a row vector of size $N=N_sN_vN_k$, by loading in the vector all the elements of the matrix scanned in a preassigned order, and $\boldsymbol{\Phi}_{m3}$ is the three-dimensional matrix of size $N_s\times N_v\times N_k$, whose element of entries (i,l,n) is given by:

$$\{\boldsymbol{\Phi}_{m3}\}_{i\,l\,n} = \frac{1}{\sqrt{N}} e^{j\left(\frac{4\pi}{\lambda}\frac{B_\perp^m}{R_i^m \sin\theta_i^m}\Delta RTE_i + \frac{4\pi}{\lambda}\Delta T^m \Delta v_l + \frac{4\pi}{\lambda}\Delta Temp^m \Delta Th_n\right)}. \tag{3}$$

In order to detect a single scatterer and to estimate its unknown elevation, deformation and thermal expansion, a Generalized Likelihood Ratio Test (GLRT) approach is used. The detection problem is formulated in terms of $K_{max}+1$ statistical hypothesis (Budillon et al., 2016). We restrict our assumption to the presence of only single scatterers ($K_{max}=1$) in the same range-azimuth resolution cell. Then, we have the following statistical hypothesis: H_0: absence of scatterers, and H_1: presence of a single scatterer. The Fast-Sup-GLRT Detector (Budillon et al., 2017a) has been recently extended to the 5D case that takes into account both thermal expansion and surface deformation (Budillon et al., 2017b); it is based on GLRT and when $K_{\max}=1$, the following binary test applies:

$$\Lambda_1'(\mathbf{u}) = \frac{\left[\mathbf{u}^H\mathbf{u}\right]}{\left[\mathbf{u}^H\left(\mathbf{I} - \boldsymbol{\Phi}_{\hat{\Omega}_1}\left(\boldsymbol{\Phi}_{\hat{\Omega}_1}^H\boldsymbol{\Phi}_{\hat{\Omega}_1}\right)^{-1}\boldsymbol{\Phi}_{\hat{\Omega}_1}^H\right)\mathbf{u}\right]} \underset{H_1}{\overset{H_{i0}}{<>}} T_1', \tag{4}$$

where $\mathbf{I}$ is the $M\times M$ identity matrix, $\boldsymbol{\Phi}_{\hat{\Omega}_1}$ is a column vector of size $M\times1$ obtained by extracting a column from $\boldsymbol{\Phi}$ and H denotes the Hermitian. The threshold T_1' can be derived by using Mote Carlo simulation and following a CFAR approach, consisting in setting T_1' in such a way to obtain an assigned probability of false alarm $P_{FA} = P\left(H_1 \middle| H_0\right)$.

4. TECHNIQUE INTER-COMPARISON

A preliminary comparison of the two abovementioned techniques was conducted over a test site located in the metropolitan area of Barcelona. The test area considered in this work covers a part of the Port of Barcelona, see the amplitude image in Figure 1. This area is covered by 61 Interferometric Wide Swath Sentinel-1 images over the period 6th March 2015 to 30 May 2017. The perpendicular baseline range is approximately 300 m, while the range of the average air temperature is 26 ºC.

The slant range resolution is 2.7 m, the resolution in azimuth is 22.5, the Rayleigh resolution in height depends on the overall orthogonal baselines span and is about 41 m.

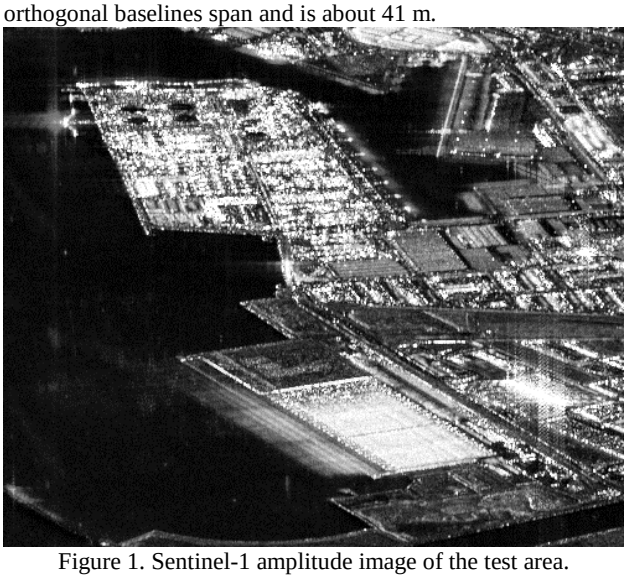

Figure 1. Sentinel-1 amplitude image of the test area.

In case of the Fast-Sup-GLRT, the thresholds have been computed by Monte Carlo simulation, fixing $P_{FA}=10^{-4}$, the search step in height is about 2 m. The spatial density of the scatterers detected by the PSI approach and the Fast-Sup-GLRT can be appreciated in Figures 2 and 3. The number of detected scatterers by the PSI approach in the study area is 8240. Over the same area, the number of scatterers detected by Fast-Sup-

GLRT is 32189. A remarkable difference in the measurements density is evident (there is a factor 4 between the two solutions). The PSI results were generated using edges *e* characterized by a high temporal gamma, with values greater than 0.7, and without performing the scatterer densification.

The Fast-Sup-GLRT results, instead, do not explicitly exploit the coherence values, but refer to a fixed probability of detecting a coherent scatterer when no scatterers are present ($P_{FA}=10^{-4}$). The two adopted criteria are quite different, so that it is very difficult to perform a comparison between the results obtained from the two methods. The inter-comparison of the results of the two techniques was computed over the set of scatterers common to both techniques. The deformation velocity maps estimated by the PSI approach and the Fast-Sup-GLRT are shown in Figures 2 and 3, respectively. The statistics of the inter-comparison (i.e. the statistics of the differences of the deformation velocity values) are:

$$\text{Mean}_{\text{VELO\_DIFF}} = 1.4 \text{ mm/yr}$$

$$\text{St.dev}_{\text{VELO\_DIFF}} = 1.2 \text{ mm/yr}$$

The mean of the velocity differences indicates a bias between the two datasets, which can be eliminated by choosing the same reference point for the velocity of the two datasets. The standard deviation of the velocity differences is close to 1 mm/yr, which is often mentioned as the precision that characterizes the PSI deformation velocity values. By assuming the same precision for the two compared techniques and uncorrelated results between the same techniques, the estimated standard deviation of the deformation velocity of each technique is:

$$\text{St.dev}_{\text{VELO\_TECHNIQUE}} = 0.85 \text{ mm/yr}$$

At the time of writing this paper, the results of the inter-comparison of the *RTE* and the thermal maps are not available. Figure 4 shows the thermal expansion map generated using the PSI approach. Most of the scatterers show negligible thermal effects (green colour), while some elements of the port show thermal effects (blue and red colours).

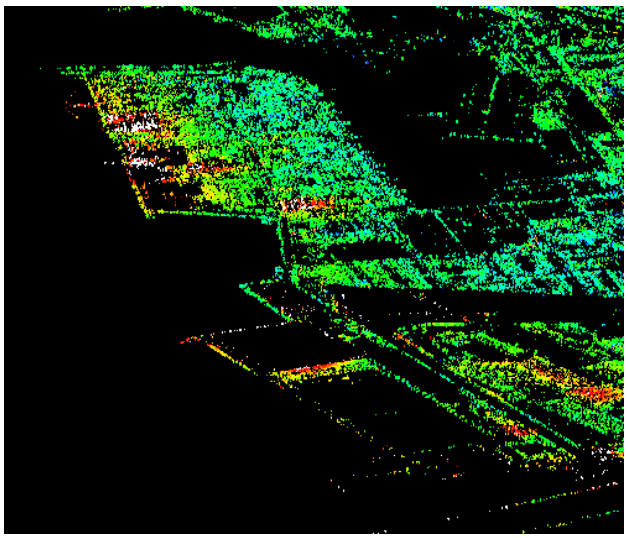

Figure 2. Deformation velocity map from Fast-Sup-GLRT. The colour scale ranges from – 10 to + 10 mm/yr.

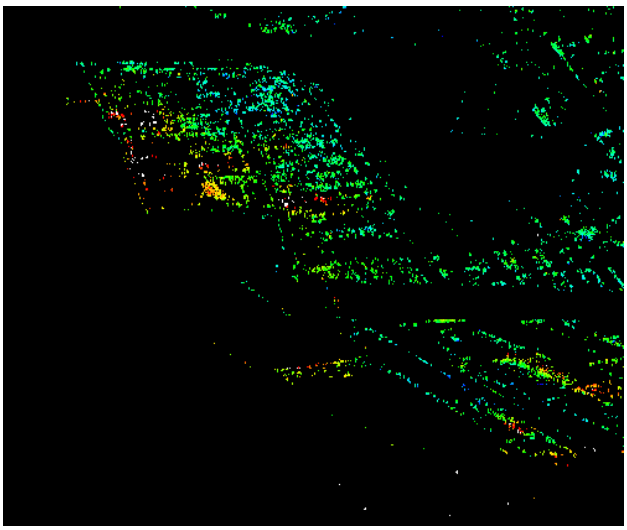

Figure 3. Deformation velocity map from the PSI approach. The colour scale ranges from – 10 to + 10 mm/yr.

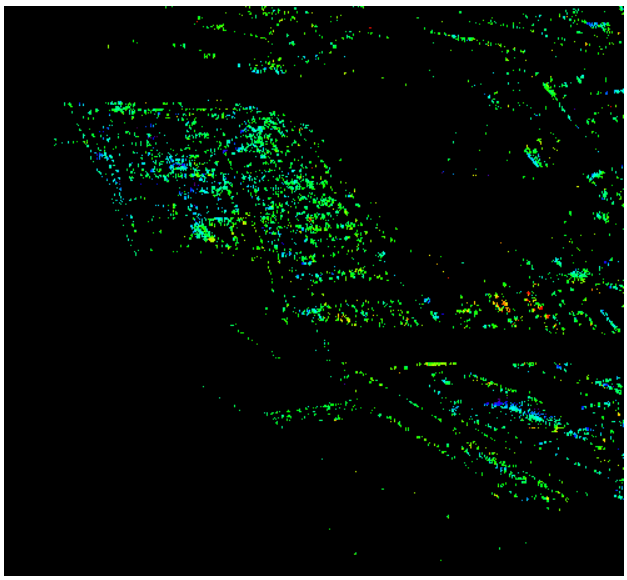

Figure 4. Thermal expansion map from the PSI approach. The colour scale ranges from – 0.5 to + 0.5 mm/ºC.

ACKNOWLEDGEMENTS

This work has been partially funded by the Spanish Ministry of Economy and Competitiveness through the DEMOS project "Deformation monitoring using Sentinel-1 data" (Ref: CGL2017-83704-P).

REFERENCES

Bamler, R., Hartl, P., 1998. Synthetic aperture radar interferometry. *Inverse Probl*, 14, pp. R1-R54.

Baselice, F., Budillon, A., Ferraioli, G., Pascazio, V., Schirinzi, G., 2014. Multibaseline SAR Interferometry from Complex Data", *IEEE J. of Selected Topics in Applied Earth Obs. and Remote Sens.*, 7(7), pp. 2911-2918.

Biescas E., Crosetto M., Agudo M., Monserrat O., Crippa B., 2007. Two radar interferometric approaches to monitor slow

and fast land deformations. *Journal of Surveying Engineering*, 133(2), pp. 66-71.

Budillon, A., Ferraioli, G., Schirinzi, G., 2014. Localization Performance of Multiple Scatterers in Compressive Sampling SAR Tomography: Results on COSMO-SkyMed Data. *IEEE J. of Selected Topics in Applied Earth Obs. and Remote Sens.*, 7 (7), pp. 2902-2910.

Budillon, A., Schirinzi, G., 2016. GLRT Based on Support Estimation for Multiple Scatterers Detection in SAR Tomography. *IEEE J. of Selected Topics in Applied Earth Obs. and Remote Sens.*, 9(3), pp. 1086-1094.

Budillon, A., Johnsy, A., Schirinzi, G., 2017a. A Fast support detector for superresolution localization of multiple scatterers in SAR tomography, *IEEE J. of Selected Topics in Applied Earth Obs. and Remote Sens.*, 10(6), pp. 2768-2779.

Budillon, A., Johnsy, A., Schirinzi, G., 2017b. Extension of a fast GLRT algorithm to 5D SAR tomography of Urban areas, *Remote Sensing*, 9(8), pp.1-21.

Crosetto, M., Monserrat, O., Iglesias, R., Crippa, B., 2010. Persistent Scatterer Interferometry: potential, limits and initial C- and X-band comparison”. *Photogrammetric Engineering & Remote Sensing*, 76(9), pp. 1061-1069.

Crosetto, M., Monserrat, O., Cuevas-González, M. Devanthéry, N., Crippa, B., 2016. Persistent Scatterer Interferometry: a review. *ISPRS Journal of Photogrammetry and Remote Sensing*, 115, pp. 78-89.

Devanthéry, N., Crosetto, M., Monserrat, O., Cuevas-González, M., Crippa, B., 2014. An approach to Persistent Scatterer Interferometry. *Remote Sensing*, 6, pp. 6662-6679.

Ferretti, A., Prati, C., Rocca, F., 2001. Permanent scatterers in SAR interferometry. *IEEE Trans. Geosci. Remote Sens.*, 39(1), pp. 8-20.

Fornaro, G., Pascazio, V., 2013. *SAR Interferometry and Tomography: Theory and Applications*. Academic Press Library in Signal Processing, Communications and Radar Signal Processing, Vol. 2, Cap. 20, pp. 1043-1117, Elsevier Ltd.

Gabriel, A.K., Goldstein, R.M., Zebker, H.A., 1989. Mapping small elevation changes over large areas: differential radar interferometry. *J. Geophys Res*, 94(B7), pp. 9183-9191.

Gernhardt, S., Bamler, R., 2012. Deformation monitoring of single buildings using meter-resolution SAR data in PSI. *ISPRS Journal of Photogrammetry and Remote Sensing*, 73, pp. 68-79.

Huang, Q., Crosetto, M., Monserrat, O., & Crippa, B. (2017). Displacement monitoring and modelling of a high-speed railway bridge using C-band Sentinel-1 data. *ISPRS Journal of Photogrammetry and Remote Sensing*, 128, pp. 204-211.

Monserrat, O., Crosetto, M., Cuevas, M., Crippa, B., 2011. The Thermal Expansion Component of Persistent Scatterer Interferometry Observations”, *IEEE Geosci. Remote Sens. Letters*, 8, pp. 864 - 868.

Reale, D., Fornaro, G., Pauciullo, A., 2013. Extension of 4-D SAR Imaging to the Monitoring of Thermally Dilating Scatterers”, *IEEE Trans. Geosci. Rem. Sens.*, 51, pp. 5296-5306.

Rosen, P.A., Hensley, S., Joughin, I.R., Li, F.K., Madsen, S.N., Rodriguez, E., Goldstein, R.M., 2000. Synthetic aperture radar interferometry. *Proceedings of the IEEE*, 88(3), pp. 333-382.

Strozzi, T., Teatini, P., Tosi, L., 2009. TerraSAR-X reveals the impact of the mobile barrier works on Venice coastland stability. *Remote Sensing of Environment*, 113(12), pp. 2682-2688.